Corrosion Science 259 (2026) 113494

Contents lists available at ScienceDirect

Corrosion Science

journal homepage: www.elsevier.com/locate/corsci

Design of rust layer stabilizers for weathering steel guided by interpretable machine learning and Bayesian optimization

Yiran Li [a,b], Lingwei Ma [a,b,c,*], Zongbao Li [a,b], Xin Guo [a,b], Jingzhi Yang [a,b], Jinke Wang [a,b], Arjan Mol [d], Dawei Zhang [a,b,c]

[a] School of Advanced Materials Innovation, University of Science and Technology Beijing, Beijing 100083, China
[b] National Materials Corrosion and Protection Scientific Data Center, University of Science and Technology Beijing, Beijing 100083, China
[c] Institute of Materials Intelligent Technology, Liaoning Academy of Materials, Shenyang 110004, China
[d] Department of Materials Science and Engineering, Delft University of Technology, Mekelweg 2, Delft 2628CD, Netherlands

ARTICLE INFO

Keywords:
Stabilization Treatment Agents
High-throughput Experiments
Interpretable Machine Learning
Weathering steel
Bayesian optimization

ABSTRACT

Surface stabilization treatment serves as a primary method to promote stable rust layer formation on weathering steel (WS). However, due to the complex and multicomponent chemical formulations of stabilization treatment agents (STA), the precise control over STA component ratios to achieve the best stabilization treatment effect remains highly challenging. This study combines high-throughput experiment and machine learning method to establish an optimization framework for designing rust layer STA formulation. By employing high-throughput droplet dispensing experiments and wire beam electrode electrochemical testing, a predictive model is constructed using the AdaBoost algorithm. Interpretability analysis is further integrated to guide Bayesian optimization for iterative formulation refinement. After two optimization cycles, the optimal STA formulation (0.70 g/L $CuSO_4$, 0.20 g/L $MgSO_4$, 0.60 g/L Na_2HPO_4, and 0.20 g/L tannic acid) is identified from over 2.8 million candidate formulations. The optimized STA promotes the generation of stable rust layer on Q420 WS, which effectively reduces rust layer defects, inhibits corrosive medium penetration, and significantly enhances the corrosion resistance of WS.

1. Introduction

Weathering steel (WS) including alloying elements such as nickel, chromium, and copper [1–4] can form a dense protective rust layer when exposed to the atmosphere, which effectively prevents extensive corrosion of the steel matrix [5–7]. However, this rust layer typically requires a relatively long formation period of about 3–10 years. During this prolonged process, sagging of rust solution and dispersion of rust particles may occur to potentially cause environmental pollution and aesthetic issues, thereby limiting the broad application of WS [8]. To accelerate the formation of rust layer on WS surface and improve its stability, researchers have developed various stabilization treatment techniques in recent years, including oxide coating treatment [9], organic–inorganic composite film treatment [10], stabilization treatment agent (STA) [11], and physical field modulation [12], all of which can enhance the compactness and stability of rust layer within a relatively short period. The application of STA has emerged as a more direct and effective method, which utilizes tailored chemical formulations to create a dense and stable rust layer on the WS surface, thereby improving both rust layer stability and environmental compatibility. For instance, Sun et al. [13] developed an STA containing $CuSO_4$, $FeSO_4$, $NaHSO_3$, NaCl, and Na_2HPO_4 for Q370qENH WS treatment. After surface treatment, the growth rate of the rust layer was twice that of the untreated sample; the main phase structure in the inner rust layer shifted from γ-FeOOH and α-FeOOH to Fe_3O_4, while the composition of the outer rust layer remained essentially unchanged. Similarly, Yu et al. [11] designed an STA for Q420 WS treatment based on an orthogonal experimental program, screening a mixture formulation of 0.25 g/L NaF, 0.75 g/L tannic acid (TA), 0.75 g/L SeO_2, and 0.50 g/L $MgSO_4$. The resulting rust layer effectively blocked atmospheric corrosive ions, thereby improving the corrosion resistance of Q420 WS.

Typically, STA for WS treatment rely on the interaction of multiple components. For instance, sulfate can accelerate the dissolution of steel matrix at the early stages of corrosion, accelerating the formation of rust layer [14]; Metallic salts containing Cu, Ni and other elements can stabilize the rust layer through the enrichment of alloy elements on the WS

* Corresponding author at: School of Advanced Materials Innovation, University of Science and Technology Beijing, Beijing 100083, China.
E-mail address: mlw1215@ustb.edu.cn (L. Ma).

https://doi.org/10.1016/j.corsci.2025.113494
Received 8 August 2025; Received in revised form 4 October 2025; Accepted 20 November 2025
Available online 25 November 2025

surface, forming local micro-cathodes that promote the formation of a dense rust layer [15,16]; Phosphate and TA can promote the rapid formation of an insoluble phosphate film and stable iron complex in the rust layer, respectively, thus enhancing the corresponding corrosion resistance [17,18]. The simultaneous use of a variety of STA components helps to further boost the growth rate and compactness of the rust layer. However, how to determine the optimal concentration and ratio within such multicomponent systems remains a major challenge.

The use of high-throughput screening (HTS) techniques has demonstrated notable screening efficiency in multicomponent systems [19,20]. For instance, we previously employed high-throughput droplet microarray screening and multi-channel electrochemical testing to determine the optimal concentration of a two-component STA for Q420 WS [21]. Both the number and size of micro-defects in outer and inner rust layers were reduced and the corrosion resistance was significantly improved. In recent years, the integration of HTS with machine learning (ML) has demonstrated significant potential in the efficient research and development of new materials. HTS enables rapid generation of large-scale experimental datasets, which provide critical support for training ML models [22–26]. Through data analysis and modeling, ML not only predicts and optimizes existing formulations to reduce experimental iterations and resource consumption, but also actively explores better new compositions within uncharted composition spaces [27–30]. For instance, Noh et al. [31] have showcased an ML-guided high--throughput experimental platform for electrolyte screening wherein ML predictions and automated experiments work in unison to efficiently screen for binary organic solvents with optimal solubility for 2,1,3-benzothiadiazole (BTZ). With this platform, they successfully identified 18 binary solvent systems with BTZ solubility surpassing 6.20 M after measuring only 218 out of 2101 candidates. In binary systems, an ML-guided HTS closed loop has identified optimal formulations with few experiments (e.g., the BTZ solubility platform). STA for the WS rust layer is a multicomponent formulation; the number of combinations rises sharply and variable relationships are more complex. Studies that pair active learning with HTS in multicomponent catalysts and in electrolyte or polymer systems show that this route is effective for multicomponent problems [32,33]. Therefore, ML-guided HTS to screen and optimize multicomponent STA for WS rust layer is a feasible approach.

This study employed a high-throughput robotic dispenser to prepare quaternary rust layer STA comprising $CuSO_4$, $MgSO_4$, Na_2HPO_4, and TA at different concentrations. High-throughput electrochemical impedance characterization was conducted using wire beam electrode (WBE) measurement. A ML model was constructed with ion concentrations of different STA components as input features and electrochemical impedance modulus value at 0.01 Hz ($|Z|_{0.01\ Hz}$) [21,34,35] as output features. After selecting the optimal model, Bayesian optimization was applied to screen optimal STA formulation ratios, followed by WBE test verification. The ML model was iteratively updated with testing results, and interpretability analysis was performed to identify STA ion concentration ranges with best performance. The optimal formulation was ultimately designed from the unknown compositional space using Bayesian optimization, which was validated through WBE impedance modulus testing. Finally, Q420 WS coupons were treated with the optimized STA and subjected to wet-dry cyclic corrosion test (CCT). The corrosion resistance and morphology of the rust layer was comprehensively analyzed using electrochemical impedance spectroscopy (EIS), scanning electron microscopy (SEM), and focused ion beam-transmission electron microscopy (FIB-TEM).

2. Material and methods

Fig. 1 illustrates the flowchart of this study, showing a high-throughput workflow integrating robotic dispenser and WBE systems for multicomponent STA preparation and characterization. Experimental data generated from this workflow are integrated with ML to build a prediction model from STA ion concentrations to rust layer

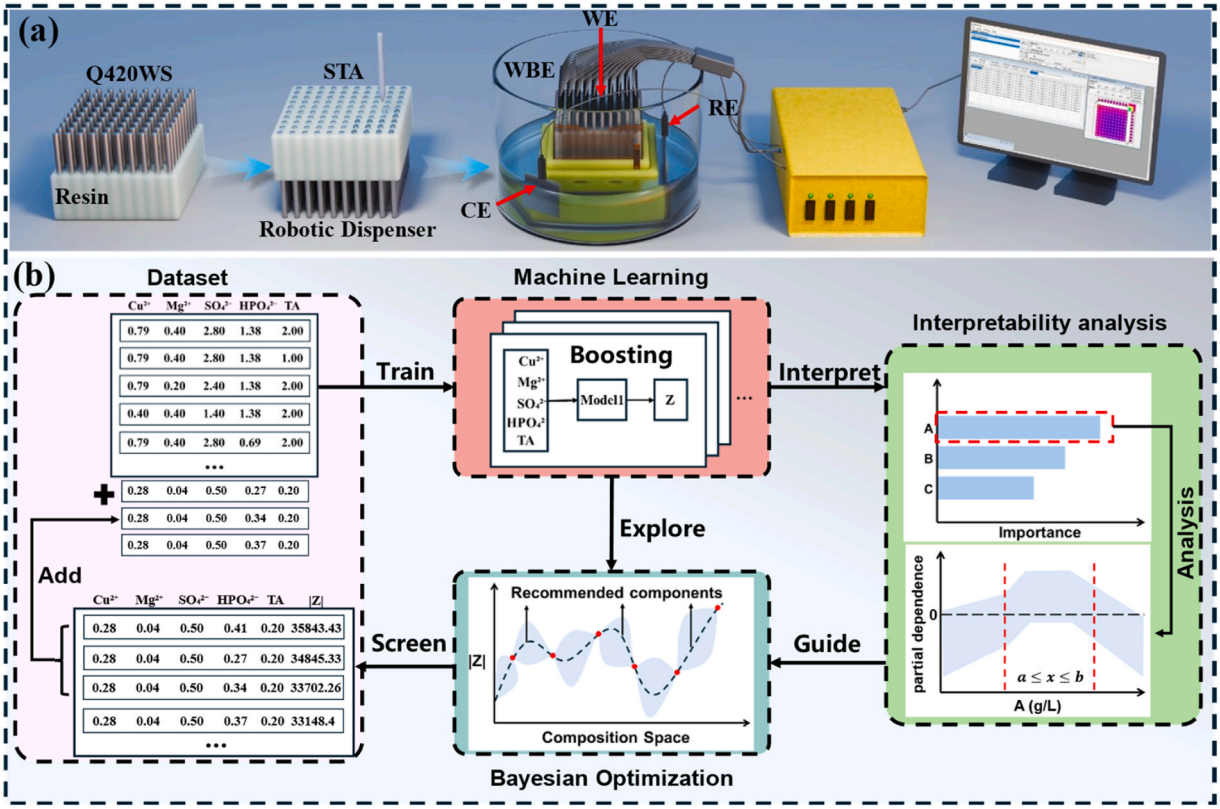

Fig. 1. Research workflow diagram: (a) High-throughput droplet dispensing experiment and WBE impedance modulus testing process; (b) ML, interpretability analysis, and Bayesian optimization for STA composition design.

impedance. Bayesian optimization was guided by interpretability analysis, and new formulations with potential excellent performance were explored in the uncharted component space. The experimental results were iteratively incorporated into the ML model to refine predictions. Through multiple cycles of modeling-experimental iterations, the accelerated and optimized STA formulation design was realized.

2.1. Material

$CuSO_4$, $MgSO_4$, Na_2HPO_4, and TA were purchased from Shanghai Morier Chemical Technology Co., Ltd., and NaCl was obtained from China National Pharmaceutical Group Chemical Reagent Co., Ltd. All reagents were used as received without further purification. Q420 WS, supplied by Nanjing Iron & Steel Group Co., Ltd. (chemical composition shown in Table 1 was determined by inductively coupled plasma optical emission spectrometry (ICP-OES, Thermo Scientific iCAP 7400, USA)), was employed to prepare both the WBE and the coupons.

2.2. WBE preparation and high-throughput surface treatment with STA

To prepare the WBE, Q420 WS was cold drawn from 5 mm to 1 mm, and cut into cylindrical rods of 30 mm. The WBE comprises 100 test channels formed from 100 of these cylinders, which were set in a template and encapsulated in epoxy resin [21]. The testing procedure, as outlined in Fig. 1**(a)**, involved three steps: (1) A robotic dispenser (GESIM Nano-Plotter 2.1, Germany) was applied to drop STA onto the WBE surface. (2) Samples were air-dried at room temperature for 24 h. (3) The WBE was integrated into an electrochemical testing system for high-throughput EIS measurement. To optimize the formulation of the quaternary STA system ($CuSO_4$, $MgSO_4$, Na_2HPO_4, and TA), a robotic dispenser was employed to prepare STA with initial concentration gradients of 0.5 g/L, ranging from 0 to 2.0 g/L (5 gradients per component). There are 625 possible combinations, and 64 formulations were selected via orthogonal experimental design for testing. High-throughput EIS was conducted to measure low-frequency impedance modulus value ($|Z|_{0.01\ Hz}$), with detailed results provided in Table S1. Since STA exists as ionic species in solution, their concentrations were converted to corresponding ion concentrations for subsequent analysis.

2.3. Experimental methods

The WBE after STA treatment was connected to a multichannel electrochemical workstation (model 910 MMA) for EIS measurements in 3.5 wt% NaCl solution over 4 h. EIS was conducted in a three-electrode system: the WBE acted as the working electrode (comprising 100 individual Q420 WS electrodes), a platinum sheet as the counter electrode, and a saturated calomel electrode (SCE) as the reference electrode. A 10 mV AC perturbation was applied around the open circuit potential. The $|Z|_{0.01\ Hz}$ for each STA composition was obtained by averaging the $|Z|_{0.01\ Hz}$ values of four parallel electrodes.

After determining the STA formulation for Q420WS surface treatment using ML method, conventional corrosion experiments were conducted to verify the effectiveness of STA in stabilizing the WS rust layer. A treatment solution (designated as solution A) was prepared by combining $CuSO_4$, $MgSO_4$, Na_2HPO_4, and TA with 3.5 wt% NaCl. A 3.5 wt% NaCl solution without additives served as the control solution. Q420 WS coupon sheets (50 mm × 70 mm × 2 mm) were placed horizontally at room temperature (298 K) and sprayed daily with either solution A or the control solution using a spray bottle. The spray application ensured complete surface coverage without liquid diffusion beyond the working area. Following five days of daily spraying, both groups underwent a dry–wet CCT to assess corrosion resistance. Each CCT cycle lasted 60 min, consisting of 12 min of immersion in 3.5 wt% NaCl solution at 45 °C and 48 min of drying at 70 °C with 70 % relative humidity. The dry–wet CCT was conducted for 10 consecutive days. After the test period, the steel coupons were collected for further analysis of rust layer stability and corrosion behavior.

For Q420 WS conventional coupons, EIS was carried out using a CS310X electrochemical workstation with the same 10 mV amplitude, using the Q420 WS coupons as the working electrode, a platinum sheet as the counter electrode, and an SCE as the reference. The surface morphologies of the Q420 WS coupons before and after the dry–wet CCT were examined by SEM (TESCAN MIRA LMS, Czech Republic; 3–5 kV for surface imaging, 10–15 kV for cross-sections; high/low vacuum as needed). Cross-sections of the rust layer and its elemental distribution were characterized by SEM with EDS (same instrument; 0° tilt, working distance ≈10 mm, 15–20 kV). The phase composition of the rust layer was determined by powder X-ray diffraction (XRD, Rigaku SmartLab SE, Japan; Cu Kα, 40 kV/30 mA; 2θ scan range of 5°–90°) and by FIB-SEM (FIB-SEM; Thermo Fisher Scientific Helios 5 CX DualBeam, USA; Pt protective cap) and TEM (TEM; Thermo Fisher Scientific Talos F200X G2, USA; 200 kV; SAED/EDS as needed).

2.4. Machine learning modeling method

In this study, the ion concentrations of the STA were used as input features and $|Z|_{0.01\ Hz}$ as the output feature to create the ML model. Four ML models (AdaBoost [36], Gradient Boosting (GBT) [37], Random Forest (RF) [38], and XGBoost [39]) were built. The resulting dataset was divided into training set and test set according to the ratio of 3:1. Hyperparameters were tuned with grid search, using mean square error as the scoring metric and giving special attention to higher-value data points (the quantile is selected as 75 %). The optimized models were evaluated with metrics such as the coefficient of determination (R^2). All random processes (data splits and model initialization) used a fixed random seed of 44; and 10-fold cross-validation was performed on the training set for model selection and evaluation. Each new experimental data was fed back to the best prediction model to complete the model iteration.

2.5. Interpretability analysis methods

The interpretability analysis of ML models primarily employs feature importance analysis and partial dependence plot (PDP). In the integrated model, feature importance is typically assessed based on each feature's contribution to information gain during the decision-making process. When a feature is used to divide nodes, it contributes a certain amount of information gain. The integrated model (such as random forest, gradient lifting tree, etc.) will accumulate the total information gain across all base learners for each feature, which serves as the feature's importance score [40]. PDP is an effective tool for interpreting the relationship between model predictions and input features [41]. By generating PDPs, it provides a visual representation of the marginal effect of one or more features on the predicted outcome, eliminating the interference of other features. Specifically, the method fixes the remaining features and varies the target feature within its value range, calculating the average predictive value to reveal the impact of this feature on the model output.

In this study, PDP method was used to investigate how each input feature affects the prediction results of the model, thereby offering a

Table 1
Chemical composition of Q420 weathering steel.

Element	C	Si	Mn	Cr	P	Ni	S	Cu	Fe
wt%	0.06	0.26	1.32	0.51	0.01	0.35	0.001	0.33	balance

more comprehensive understanding of the model's behavior and key factors. To this end, the Partial Dependence Display module in the scikit-learn library is applied to generate PDPs for each feature and capture possible exceptions that may occur during the plotting process, ensuring the integrity and accuracy of the analysis.

$$\mathrm{PDP}(X_j) = \frac{1}{n}\sum_{i=1}^{n}\widehat{f}(X_i^c, X_j) \tag{1}$$

n is the sample size, $\widehat{f}(X)$ is the ML model, X_i^c represents the all features of i, except X_j, (X_i^c, X_j) denotes the feature vector of sample i where all other features are held constant, and feature X_j is varied across its possible values.

2.6. Bayesian optimization method

In composition design, Bayesian optimization constructs an alternative model to approximate the relationship between the objective function and the compositional variables [42]. It then uses an acquisition function to guide the selection of the next experimental point, enabling efficient exploration of the optimal combination with fewer experiments [43,44].

In this study, AdaBoost is employed as the regression model to approximate the objective function, and the predicted performance value is used as an estimate of the current compositional combination. The acquisition function chosen is Expected Improvement (EI), with the following formula:

$$EI = \sigma[\varphi(z) + z\phi(z)] \tag{2}$$

$\varphi(z)$ and$\phi(z)$ denote the standard normal probability density function and cumulative distribution function, respectively. $Z = (\mu - \mu*)/\sigma$,$\mu*$represents the best observed value in the current dataset, μ represents the mean value of current distribution, σ represents the variance of the current distribution. To compute EI, we used an AdaBoost regression surrogate. At each BO iteration, B = 50 AdaBoost models were trained on bootstrap resamples of the current data; the predictive mean μ(x) was the ensemble average and the predictive uncertainty σ(x) was the sample standard deviation of the ensemble predictions, augmented by an observation-noise term equal to the validation RMSE.

3. Results and discussion

3.1. STA preparation and characterization

The selection of $CuSO_4$, $MgSO_4$, Na_2HPO_4, and TA as the STAs were based on the synergistic effects of these constituents in promoting the formation of α-FeOOH, enabling alloy-element enrichment, forming protective iron phosphate and iron tannate films, and inhibiting chloride-ion attack. Fig. 2 presents the correlation analysis results of different STA ion concentrations and $|Z|_{0.01\ Hz}$ values for the 64 samples obtained from the WBE testing, the distribution range of $|Z|_{0.01\ Hz}$ ranged from 11.8 kΩ·cm^2 to 24.4 kΩ·cm^2. To evaluate the contribution of individual components to the overall system performance, 5 out of the 64 formulations included only one single component and were specifically selected. Single-component $|Z|_{0.01\ Hz}$ ranged 13.8–21.7 kΩ·cm^2, but the optimal multicomponent reached 24.4 kΩ·cm^2, showing that only tuned combinations achieve the target performance. According to the scatter plots and histograms of ion concentration distribution, the concentrations of Cu^{2+}, Mg^{2+}, SO_4^{2-}, HPO_4^{2-}, and TA exhibited relatively uniform distributions, while $|Z|_{0.01\ Hz}$ followed an approximately normal distribution.

Therefore, the orthogonal experimental design can effectively extract the representative concentration ratios with a well-distributed dataset, which is suitable for subsequent ML modeling. With the increase of Cu^{2+} and SO_4^{2-} concentrations, $|Z|_{0.01\ Hz}$ values initially

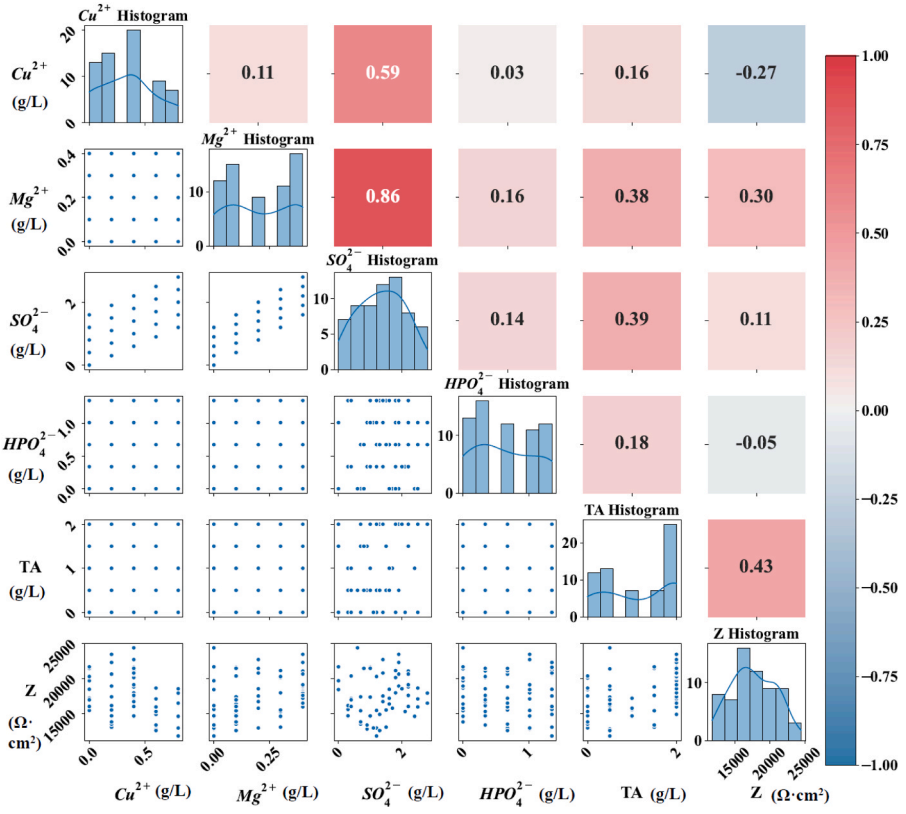

Fig. 2. Distribution and correlation matrix of different ion concentrations and electrochemical impedance. The diagonal shows histograms for each ion and $|Z|_{0.01\ Hz}$, the lower-left shows pairwise scatter plots, and the upper-right shows the correlation matrix (positive in red, negative in blue, deeper colors = stronger).

increased then decreased, indicating that there is an optimal concentration range of Cu^{2+} and SO_4^{2-}. In contrast, other ions showed no significant correlation with $|Z|_{0.01\ Hz}$. Correlation analysis demonstrates varying relationships between ion concentrations and $|Z|_{0.01\ Hz}$: TA and Mg^{2+} exhibited positive correlations with $|Z|_{0.01\ Hz}$, whereas Cu^{2+} displayed a negative correlation. It should be pointed out that the correlation analysis can only reveal the overall trend between ion concentration and $|Z|_{0.01\ Hz}$, and the specific optimal concentration interval requires further analysis and investigation by subsequent interpretable ML methods.

3.2. ML modelling and iteration

After converting the concentrations of different STA formulations into corresponding ion concentrations and defining ion concentrations as input features with $|Z|_{0.01\ Hz}$ as the output feature, four ML models (AdaBoost, GBT, RF, and XGBoost) were constructed. The training set and the test set were divided according to the ratio of 3:1 for performance evaluation. Fig. 3**(a-d)** display the prediction scatter plots for the four models respectively. It can be observed that the prediction results of the training set are close to the ideal diagonal in the four models, indicating that the models can effectively capture the overall distribution patterns of the dataset in the fitting process. However, in the prediction results of the test set, there are obvious differences among the models. The Fig. 3**(e-f)** shows that the training set of AdaBoost achieves R^2 of 0.82, second to XGBoost at 0.92. On the test set, AdaBoost achieves R^2 of 0.66, higher than RF at 0.56, GBT at 0.57 and XGBoost at 0.55. The R^2 drop from training to test for AdaBoost is 0.16, whereas XGBoost drops by 0.37 and RF drops by 0.23, demonstrating better generalization of AdaBoost. The scatter distribution of AdaBoost model is the closest to the diagonal, indicating the highest overall prediction accuracy. In contrast, the distribution of prediction points of RF and GBT models on

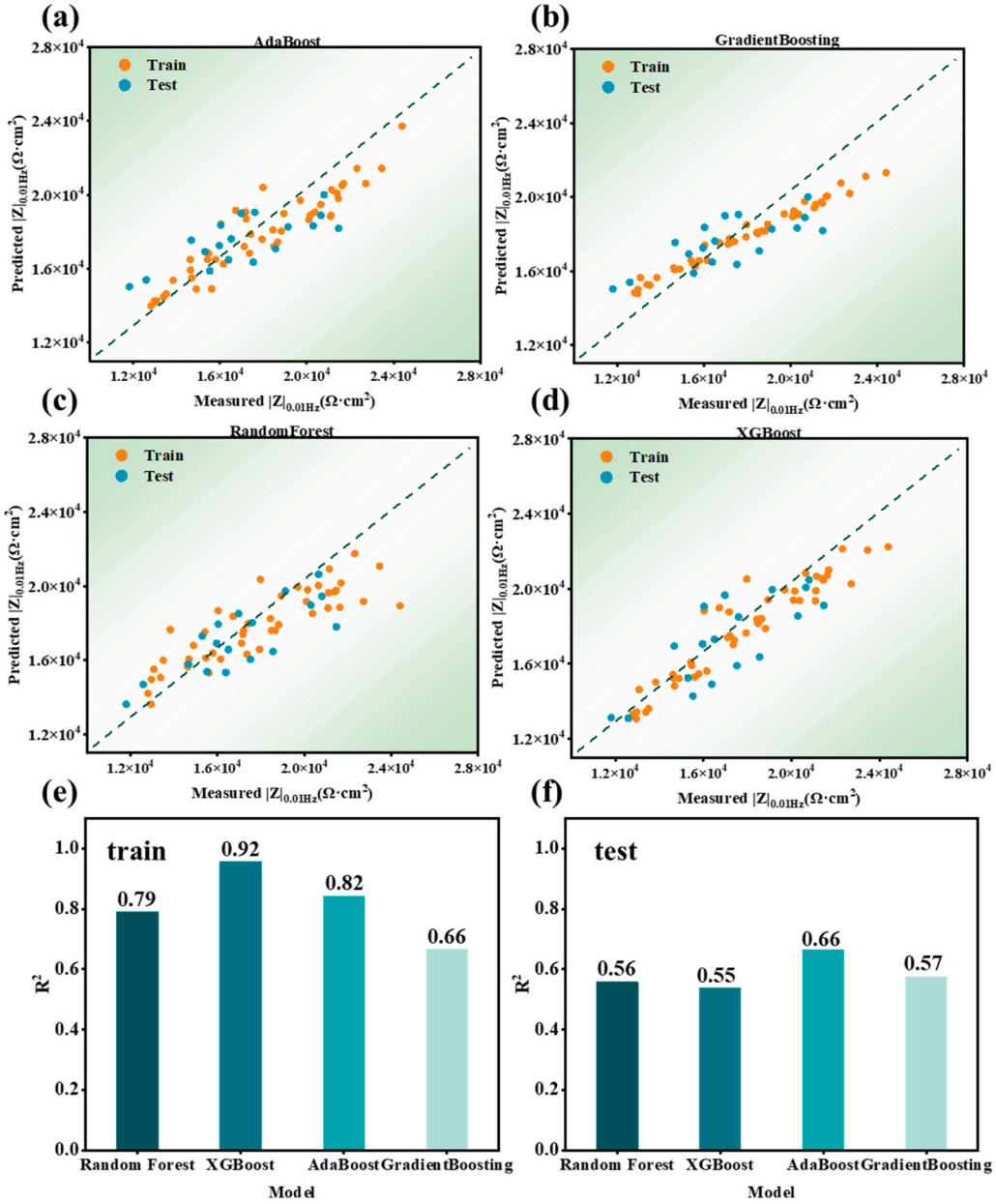

Fig. 3. Comparison of ML model prediction performance on training set and test set: (a) prediction scatter plots of (a) AdaBoost model, (b) GBT model, (c) RF model, (d) XGBoost model; (e) training set and (f) test set precision accuracy bar charts of four ML models. The scatter plots show the relationship between predicted and actual values. The bar charts display the R^2 for each model; higher values indicate better fitting performance.

the test set is slightly scattered, and there is a prediction bias for localized samples. Although the accuracy of XGBoost in the training set is higher than that of the AdaBoost model, the prediction accuracy of XGBoost in the test set is lower with an over fitting phenomenon. According to the results of model selection and prediction performance comparison, AdaBoost delivers the most accurate predictions of the four ML models, and is therefore chosen for subsequent concentration optimization and experimental verification.

The main objective of this study is to identify the optimal concentration ratios for rust layer STA, therefore Bayesian optimization is used to supplement the data. By iteratively supplementing new experimental data, particularly data of formulations that result in high corrosion resistance (high $|Z|_{0.01\ Hz}$ values from the EIS measurement), the prediction accuracy of the model in the high corrosion resistance region can be continuously improved. This targeted data supplement enables the model to capture potential STA formulations with high corrosion resistance across broader parameter spaces. Bayesian optimization can significantly accelerate the search for maxima in high-dimensional spaces, so as to quickly locate the candidate concentration ratios that may have the optimal corrosion resistance within a limited number of experiments. It is screened in the concentration ratio space where the concentration gradient is subdivided into 0.1 g/L intervals, yielding a sample space of 194,481 (21^4), and the 10 formulations with the highest expected performance were prepared for electrochemical test. The prediction results and test results are shown in Table 2. These supplementary data were included in the original dataset for the first round of model iteration. Fig. 4**(a)** shows the prediction scatter diagram of the model after first round of iteration, and both the training set and test set data are closer to the ideal diagonal. The circled region marks the new data points, which cluster mainly above 27.0 kΩ·cm^2, and the highest predicted value is 28.5 kΩ·cm^2. After adding targeted data and retraining, test R^2 rose from 0.70 to 0.85 and train R^2 from 0.85 to 0.89, indicating better accuracy and generalization in the high-performance region and a firmer basis for concentration optimization.

3.3. Component design guided by interpretability analysis

After completing the first round of iteration, the interpretability analysis of the constructed model including feature importance analysis and partial dependence analysis was carried out to further explore the contribution of each ion to the impedance modulus value and how the impedance responds across different concentration ranges. By feature importance analysis, we can intuitively understand the influence weighting of each ion and its contribution to the prediction results of the model, while the PDP further reveals how different ion concentrations affect the impedance modulus value within a specific range. Together these insights offer a clearer rational basis for the subsequent fine concentration regulation and the confirmation of the optimal component ratio.

Fig. 5**a** presents the results of feature importance analysis. It can be seen that the importance ranking results are SO_4^{2-}>Cu^{2+}>HPO_4^{2-}>TA>Mg^{2+}, indicating that SO_4^{2-} and Cu^{2+} ions have the highest contribution to the model prediction. Fig. 5**(b–f)** presents the PDP results for the five different types of ions. The analysis reveals that the $|Z|_{0.01\ Hz}$ value reaches an optimum within a specific concentration range for both SO_4^{2-} and Cu^{2+}; once either ion exceeds that range, the $|Z|_{0.01\ Hz}$ value declines. By contrast, changing the concentrations of Mg^{2+}, HPO_4^{2-}, or TA ions produces only slight $|Z|_{0.01\ Hz}$ variations with no clear optimum interval. Hence, it is necessary to pay attention to the optimal concentration ratio of SO_4^{2-} and Cu^{2+} within their respective optimal concentration ranges. For SO_4^{2-}, the partial dependence curve peaks at the concentration of 0.4–0.6 g/L, while Cu^{2+} shows a $|Z|_{0.01\ Hz}$ peak at the concentration of 0.2–0.5 g/L. Subsequent formulation optimization will therefore confine SO_4^{2-} and Cu^{2+} to these ranges. In the second Bayesian-optimization round, the step was refined to 0.05 g/L (search space 41^4 = 2825,761), and an AdaBoost base model with an EI criterion was again used to screen high-resistance STA candidates.

The five formulations with the highest EI values were prepared again for WBE testing (Table 3). These supplementary data were merged with the original dataset for the second round of model iteration. As shown in Fig. 6**(a)**, the scatter distribution of both the training set and test set is closer to the ideal diagonal, while the newly added $|Z|_{0.01\ Hz}$ data cluster mainly above 30.0 kΩ·cm^2. Compared with the first iteration, the R^2 values for the test and training sets increased from 0.85 and 0.89–0.93 and 0.94, demonstrating that narrowing the concentration ranges and supplementing high $|Z|_{0.01\ Hz}$ data markedly boost the predictive accuracy and generalization. Among the five formulations, the optimal STA composition is 0.70 g/L $CuSO_4$, 0.20 g/L $MgSO_4$, 0.60 g /L Na_2HPO_4, and 0.20 g/L TA. The highest predicted low-frequency impedance modulus value reaches 35.8 kΩ·cm^2, with a test value of 35.8 kΩ·cm^2. Compared to the maximum value obtained from the initial orthogonal experimental design (24.4 kΩ·cm^2), this represents a 47.0 % improvement, achieved with only 79 (64 + 15) experiments. This concentration ratio was then applied to treat Q420 WS coupon samples, followed by experimental characterization to verify the effectiveness of the selected rust layer STA and clarify its stabilization mechanism.

3.4. Electrochemical testing of Q420 WS coupons

The Q420 WS coupon was sprayed with a solution containing 0.70 g/L $CuSO_4$, 0.20 g/L $MgSO_4$, 0.60 g/L Na_2HPO_4, and 0.20 g/L TA in 3.5 wt % NaCl, serving as the pre-treated sample. The blank sample was prepared by spraying Q420 WS coupon with 3.5 wt% NaCl solution. After five days of surface treatment, both samples underwent 10 days of wet-dry CCT, and EIS measurements were conducted before and after the CCT process. EIS can effectively evaluate the protective performance of the rust layer. Nyquist plots and Bode plots of blank and pre-treated samples, before and after dry-wet CCT are shown in Fig. 7**(a-c)**. Before the accelerated CCT test, the electrochemical process is controlled by two factors: the electrical double-layer structure and the corrosion-product film. Accordingly, the equivalent electric circuit (EEC) of R(Q(R(QR))) was applied to fit the EIS data, as depicted in Fig. 7**d** [45]. After 10 days of dry–wet CCT, the electrochemical process is controlled by three factors: the electrical double layer, the corrosion-product film, and diffusion resistance [46–49]. Consequently, the EEC of R(C(R(Q(RW)))) was selected to fit the EIS data, as shown in Fig. 7**e** [50]. R_s, R_r, and R_{ct} denote the solution resistance, the resistance of the rust layer, and the charge transfer resistance, respectively. C_r is the ideal capacitance of the rust layer, Q_{dl} and n_{dl} are the constant phase element parameters relative to the double layer capacitance, and W represents the Warburg impedance, which represents the diffusion of oxygen to the interface between the substrate and the rust layer [10,51,52]. The fitted parameters are listed in Table 4, and the R_r and R_{ct} values are utilized to represent the corrosion resistance of the WS surface. Before cyclic dry-wet CCT, the R_r values of the blank and pre-treated Q420 WS specimens was 36.1 Ω·cm^2 and 32.9 Ω·cm^2, with corresponding R_{ct} of 1199.5 Ω·cm^2 and 827.6 Ω·cm^2; the lower initial R_{ct} of the pre-treated sample implies a lower

Table 2
Experimental results from the first cycle of Bayesian optimization.

$CuSO_4$ (g/L)	$MgSO_4$ (g/L)	Na_2PHO_4 (g/L)	TA (g/L)	Prediction|$Z\|_{0.01\ Hz}$ (kΩ·cm^2)	Test|$Z\|_{0.01\ Hz}$ (kΩ·cm^2)
0.8	0.2	0.2	0.5	28.5	28.8
0.8	0.1	0.1	0.7	28.4	27.8
0.8	0.1	0.2	0.5	28.4	29.1
0.8	0.1	0.1	0.5	27.5	27.3
0.8	0.1	0.2	0.4	28.4	26.1
0.8	0.1	0.1	0.4	27.5	27.6
0.8	0.1	0.2	0.3	28.4	29.4
0.9	0.1	0.2	0.3	28.4	30.9
0.9	0.1	0.2	0.5	28.4	29.4
0.9	0.1	0.2	0.7	28.4	27.2

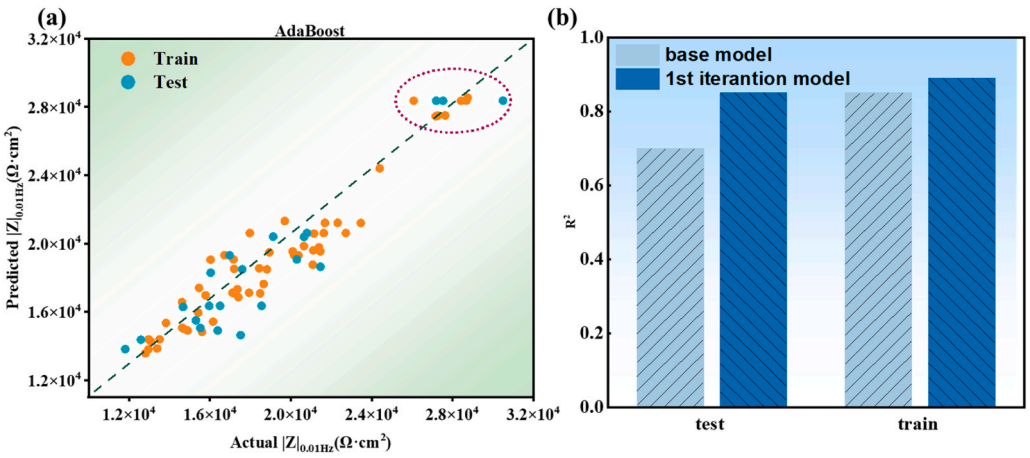

Fig. 4. AdaBoost model prediction results after the first cycle of supplemental experimental data: (a) Scatter plots of predicted vs. actual values (the purple circle shows the newly added data points selected through Bayesian optimization); (b) Model prediction accuracy comparison before and after the first cycle of iteration.

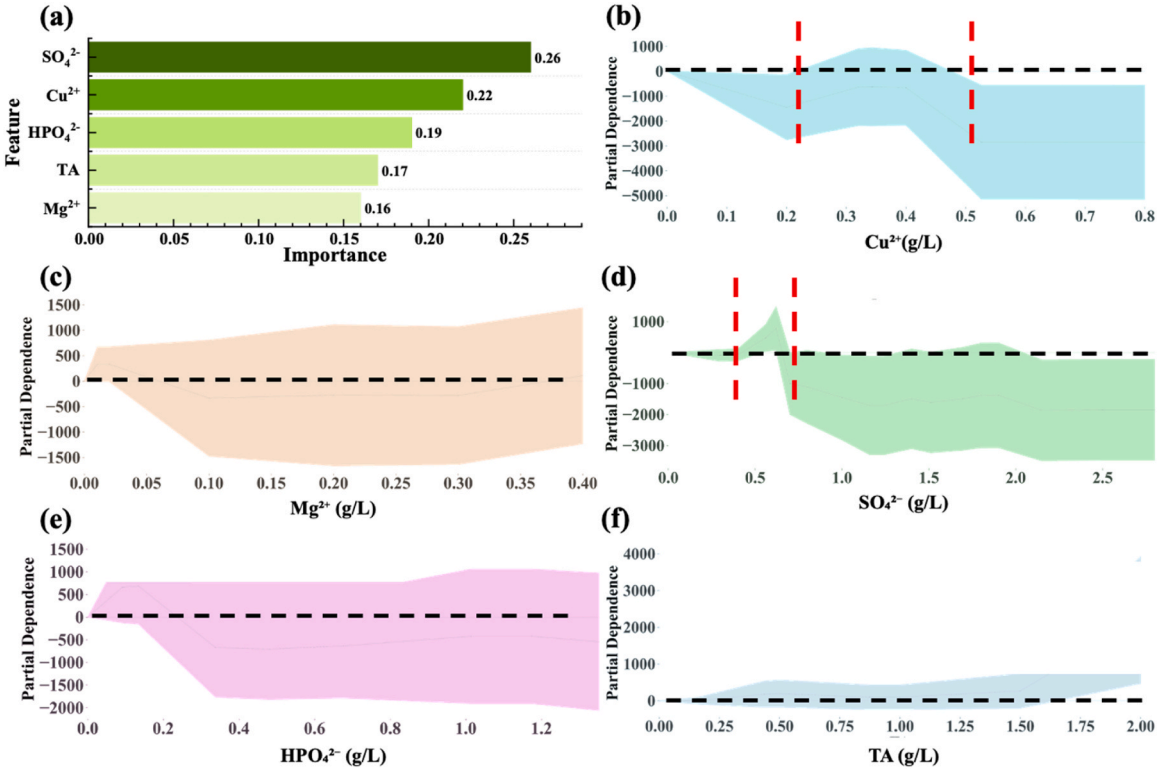

Fig. 5. ML interpretability analysis results: (a) Feature importance analysis; PDPs of (b) Cu^{2+}, (c) Mg^{2+}, (d) SO_4^{2-}, (e) HPO_4^{2-}, and (f) TA. The x-axis indicates the concentration of each ion or TA, while the y-axis represents the model's response trend to the variable. Shaded areas denote confidence intervals, and purple dashed cycles in (b) and (d) highlight the concentration ranges that have a critical influence on $|Z|_{0.01\ Hz}$ values.

Table 3
Experimental results from the second cycle of Bayesian optimization.

$CuSO_4$ (g/L)	$MgSO_4$ (g/L)	Na_2PHO_4 (g/L)	TA (g/L)	Prediction $\|Z\|_{0.01\ Hz}$ (kΩ·cm²)	Test $\|Z\|_{0.01\ Hz}$ (kΩ·cm²)
0.70	0.20	0.55	0.20	33.5	33.1
0.70	0.20	0.40	0.20	35.8	34.8
0.70	0.20	0.45	0.20	33.5	33.7
0.70	0.20	0.50	0.20	32.7	33.1
0.70	0.20	0.60	0.20	35.8	35.8

resistance to redox reactions at the steel surface, resulting in early rust formation. After CCT measurement, the rust layer had been stabilized, and the R_r values change to 31.2 Ω·cm² and 72.6 Ω·cm² for the blank Q420 WS coupon and the treated one, respectively. While R_{ct} fell to 19.2 Ω·cm² and 26.9 Ω·cm², respectively. The combination of a higher final R_r and a lower final R_{ct} shows that the pre-treated coupon developed a denser, more protective rust film and, once stabilized, displayed better corrosion resistance than the blank coupon sample [45].

3.5. Rust layer analysis of Q420 WS coupons after dry-wet CCT

Fig. 8 presents the cross-sectional SEM images and corresponding EDS results for the rust layers on the blank and pre-treated Q420

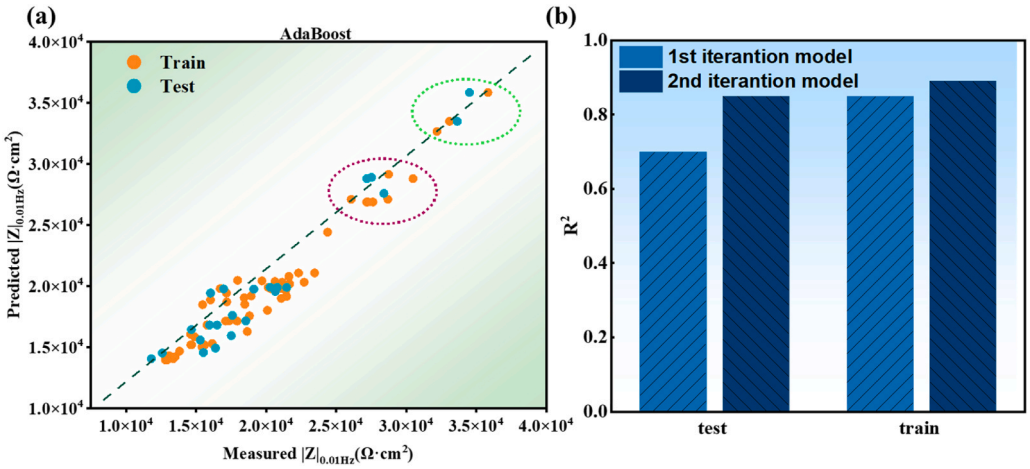

Fig. 6. AdaBoost model prediction results after the second cycle of supplemental experimental data: (a) scatter plots of predicted vs. actual values (the purple circle shows the newly added data points selected through Bayesian optimization); (b) Model prediction accuracy comparison after the second iteration vs. first iteration.

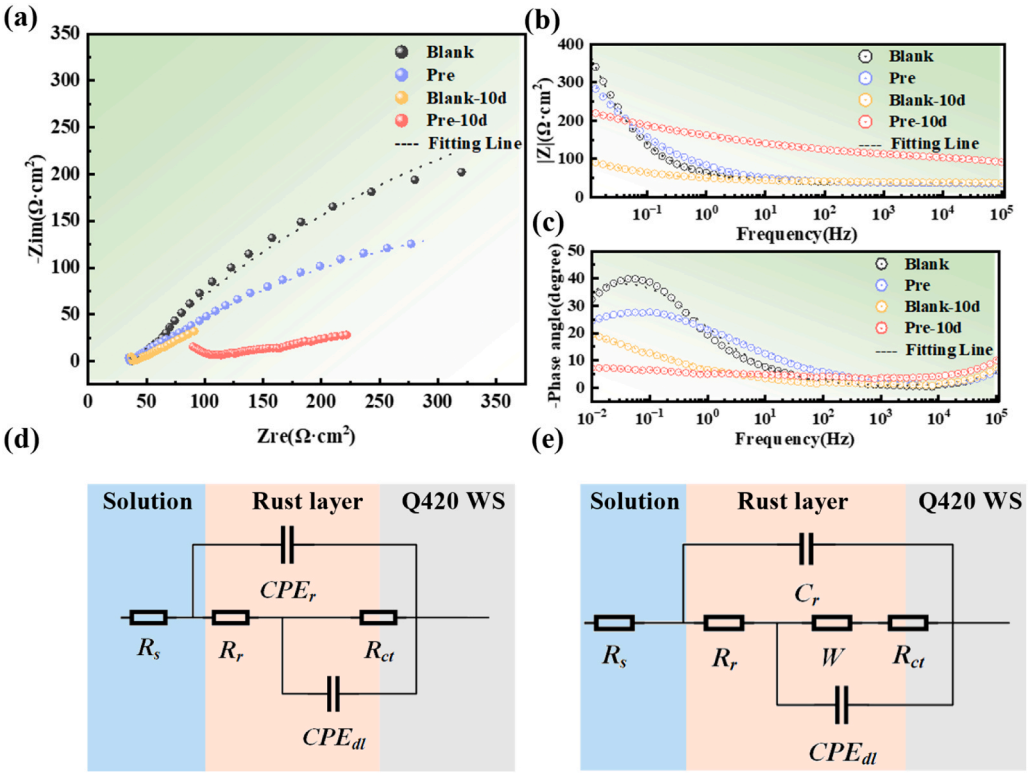

Fig. 7. EIS results of the rust layer on Q420 WS coupons for blank sample and pre-treated sample before and after dry-wet CCT experiments: (a) Nyquist plots; (b) Bode impedance diagram; (c) phase angle diagram; EEC used to fit the EIS data: (d) before and (e) after dry-wet CCT experiments.

Table 4
Fitting parameters of electrochemical curves after different treatments.

Means of treatment	R_r ($\Omega\cdot cm^2$)	$C_r/Q_r\times 10^{-9}$ ($\Omega^{-1}\cdot cm^{-2}\cdot s^n$)	n_r	R_{ct} ($\Omega\cdot cm^2$)	W ($\Omega\cdot cm^2$)	$Q_d\times 10^{-2}$ ($\Omega^{-1}\cdot cm^{-2}\cdot s^n$)	n_d	χ^2
Blank	36.1	473	0.67	1199.5	–	1.13	0.58	2.13×10^{-4}
Pretreatment	32.9	6.77	0.98	827.6	–	0.85	0.44	2.75×10^{-4}
Blank 10d-CCT	31.2	7.38	–	19.2	1.38×10^{-2}	2.93	0.30	7.69×10^{-5}
Pretreatment 10d-CCT	72.6	2.55	–	26.9	1.27×10^{-5}	9.45	0.12	7.09×10^{-5}

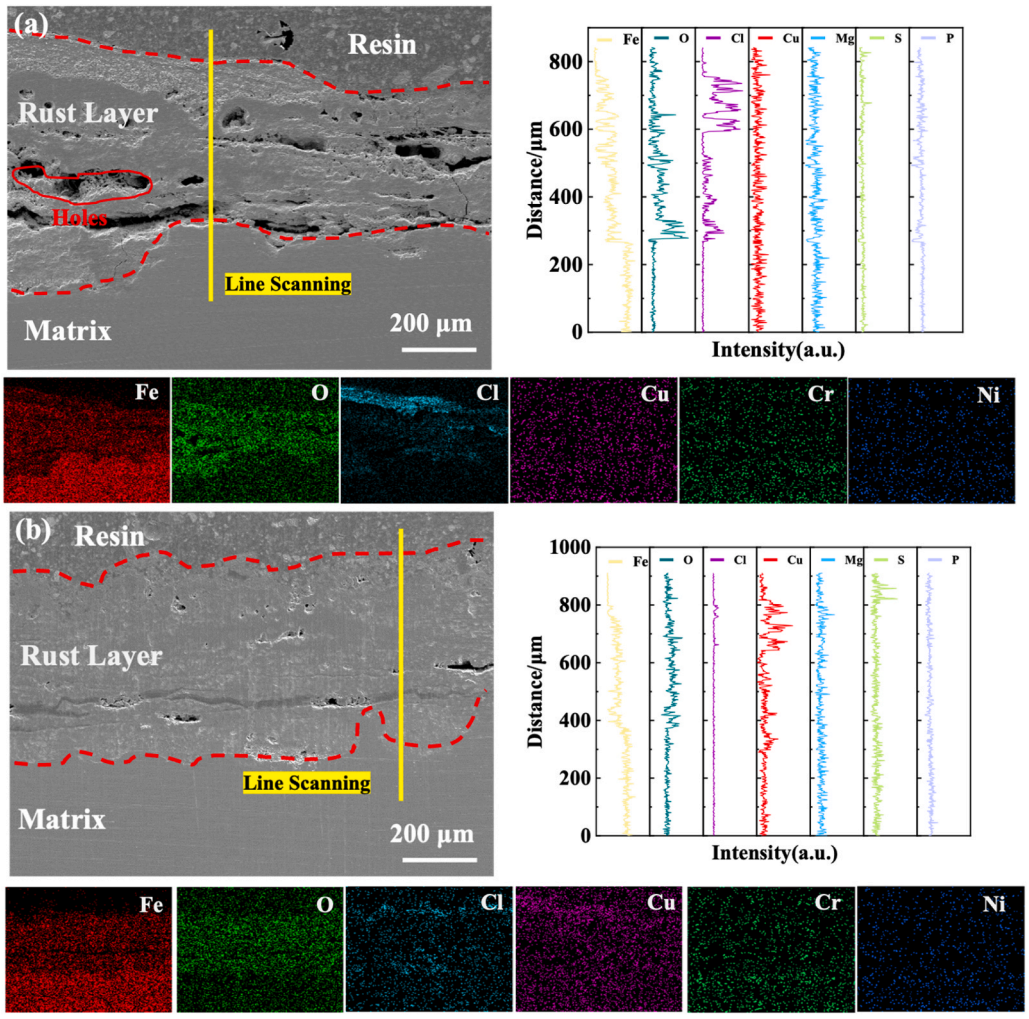

Fig. 8. Cross-sectional SEM images, line-scan analysis, and EDS results of (a) the blank sample and (b) the pre-treated sample after 10 days of dry-wet CCT.

coupons after 10 days of dry-wet CCT measurement. As shown in Fig. 8 **(a)**, there are a large number of holes and cracks in the rust layer of the blank sample. By contrast, Fig. 8**(b)** shows that surface stabilization markedly reduces the holes and defects in the pre-treated sample, which verifies that the STA treatment can fill the holes and improve the compactness of the rust layer. From the perspective of elemental distribution, surface mapping results reveal spatial variations in elemental composition across the rust layer. Cu enrichment was observed in the rust layer of the pre-treated sample, which was mainly distributed at the outer region of the rust layer. The presence of Cu enhances both the compactness and the corrosion resistance of the rust layer [53].

For the blank sample, pronounced Cl^- accumulation appears at the rust layer, indicating that the rust layer cannot effectively prevent the penetration of chloride ions. In contrast, no Cl^- enrichment was detected in the rust layer of the pre-treated sample, demonstrating that the application of STA suppressed further intrusion of corrosive media and stabilized the formation of the rust layer. In order to more clearly show the difference of element distribution between the blank sample and the pre-treated sample with STA, line-scan analyses were performed across the cross-sections of both samples. The results confirm again that after the STA treatment, Cu and S elements were enriched in the outer rust layer of the pre-treated sample, and the chloride ion content was significantly lower than that of the blank sample.

Fig. 9**(a_1–f_1)** shows the surface morphology of the rust layer on the blank and pre-treated samples before the CCT, and Fig. 9**(a2–f2)** presents the same samples after 10 days of CCT measurement. The blank sample features a loose, porous structure with micro-cracks, dominated by fine, powdery γ-FeOOH phase structure [54]. The pre-treated sample also contains some γ-FeOOH phase but has already begun to form the more stable, comparatively compact α-FeOOH phase [54]. In the XRD results shown in Fig. 10, the presence of the γ-FeOOH phase and the α-FeOOH phase is also confirmed. After 10 days of CCT, the rust layer for the blank sample remains largely composed of porous γ-FeOOH, whereas the pre-treated sample develops spiky, thick-plate α-FeOOH with sharp edges, yielding a denser and more stable rust layer [54]. The experimental results confirm that the effective surface stabilization treatment using the rust layer STA promotes the formation of the stable, corrosion resistant α-FeOOH phase. This treatment facilitates the formation of a denser rust layer, reduces the occurrence of holes and cracks, and consequently delivers superior corrosion resistant property.

To further quantify the amount of different phase structures in the rust layer, XRD was performed on the blank and pre-treated samples after 10 days of dry-wet CCT, as shown in Fig. 10. Because the relative intensities and peak widths in the XRD patterns reflect the phase composition of iron oxides, semi-quantitative analysis was performed using the relative intensity ratio (RIR) method [49]. XRD peaks at 21.4°, 33.4°, and 36.7° were assigned to α-FeOOH; peaks at 14.3°, 27.1°, and 36.7° were assigned to γ-FeOOH; and peaks at 30.4°, 35.8°, and 43.4° corresponded to Fe_3O_4/γ-Fe_2O_3 [55]. The semi-quantitative results in Fig. 10**(b)** show that the pre-treated sample contains a higher proportion of the stable α-FeOOH phase and a lower proportion of γ-FeOOH compared with the blank sample. In addition, during wet–dry cycling

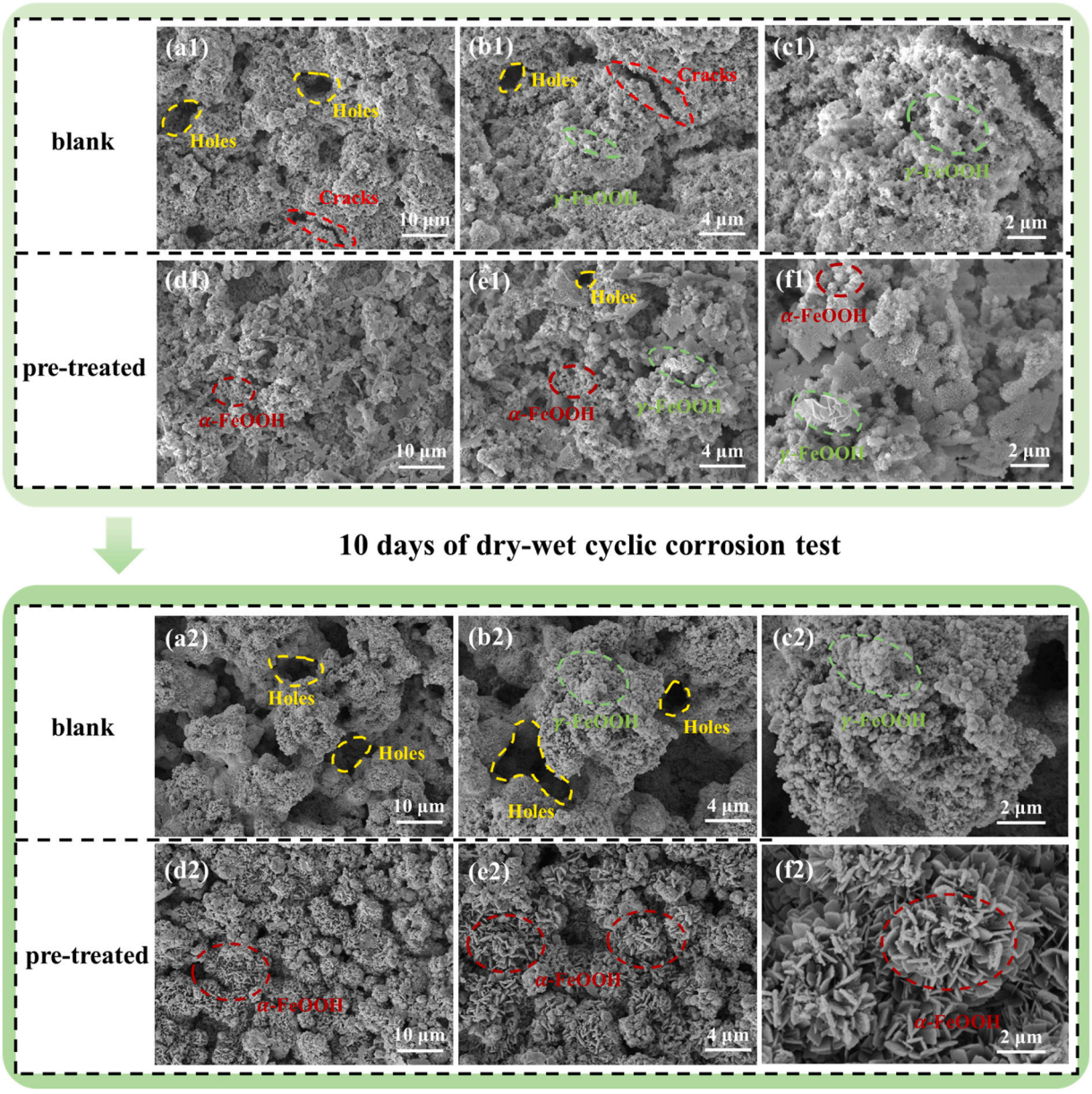

Fig. 9. Surface SEM morphologies of rust layer before and after CCT: (a1-c1) Blank sample before CCT; (d1-f1) Pre-treated sample before CCT; (a2-c2) Blank sample after CCT; (d2-f2) Pre-treated sample after CCT.

the loose outer rust layer tends to spall, and we sampled the relatively compact inner rust layer; therefore, we didn't detect the β-FeOOH. These findings demonstrate that the pre-treated sample possesses superior corrosion resistance, reflected by the increased content of stable α-FeOOH phase and the reduced presence of unstable phases.

3.6. TEM analysis of the rust layer on Q420 WS coupons after dry-wet CCT

To investigate the nanoscale structure of the rust layer, cross-sectional regions from both blank and pre-treated samples, after 10 days of CCT, were selected for TEM analysis. The cross-sections of rust layer were sampled using FIB techniques. Numerous microcracks and micropores are present along the depth direction of the cross-section image of a blank sample (Fig. 11**(c)**). In comparison, the cross-section of the pre-treated sample shows a significant reduction in microcracks (Fig. 12**(c)**). Based on the selected-area electron diffraction (SAED) analysis in Fig. 11**(f)**, the bright-field TEM image of the blank sample (Fig. 11**(e)**) reveals key phase identifications: the red-marked regions in Fig. 11**(g)** and Fig. 11**(h)** correspond to α-FeOOH, with lattice spacing of 0.230 nm and 0.269 nm, which match the (200) and (130) crystal planes [56,57], respectively. Meanwhile, regions in Fig. 11**(i)** and Fig. 11**(j)** are identified as γ-FeOOH, with lattice spacing of 0.243 nm and 0.173 nm, corresponding to the (041) and (151) crystal planes [56], consistent with the crystal structures observed in the XRD results. The TEM images of the pre-treated sample reveal that the rust layer was primarily composed of rod-like and densely packed nanocrystals with size less than 15 nm, resulting in a more uniform and compact structure. According to the SAED pattern in Fig. 12**(f)**, these nanocrystals are identified as α-FeOOH, with lattice spacing of 0.208 nm, 0.151 nm, 0.192 nm and 0.269 nm, corresponding to the (220), (310), (041) and (130) crystal planes, respectively [56,57]. A comparison between the SAED patterns of the blank and pre-treated samples shows that the pre-treated one exhibits significantly higher crystallinity [58,59]. The enhanced crystallinity improves the protective performance of the rust layer, as a dense and orderly crystal structure can more effectively block

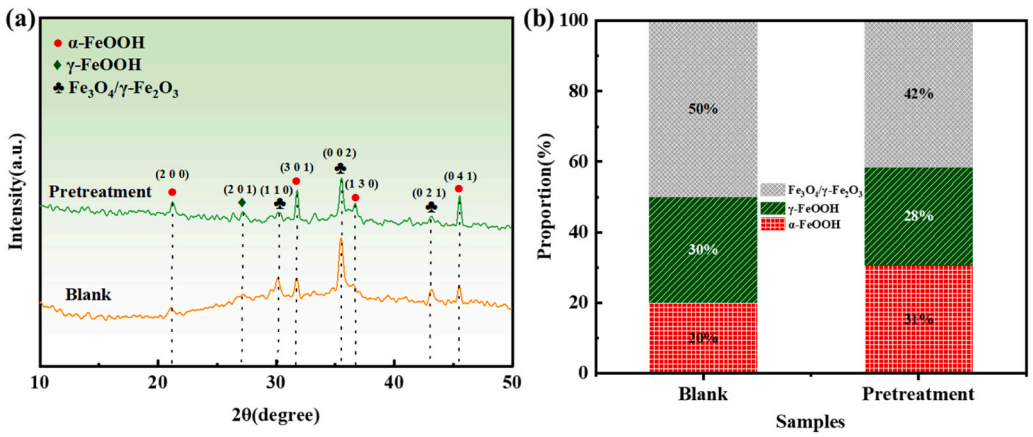

Fig. 10. (a) XRD analysis of blank and pre-treated samples after dry-wet CCT; (b) semi-quantitative analysis of phase composition of corrosion products in the rust layer.

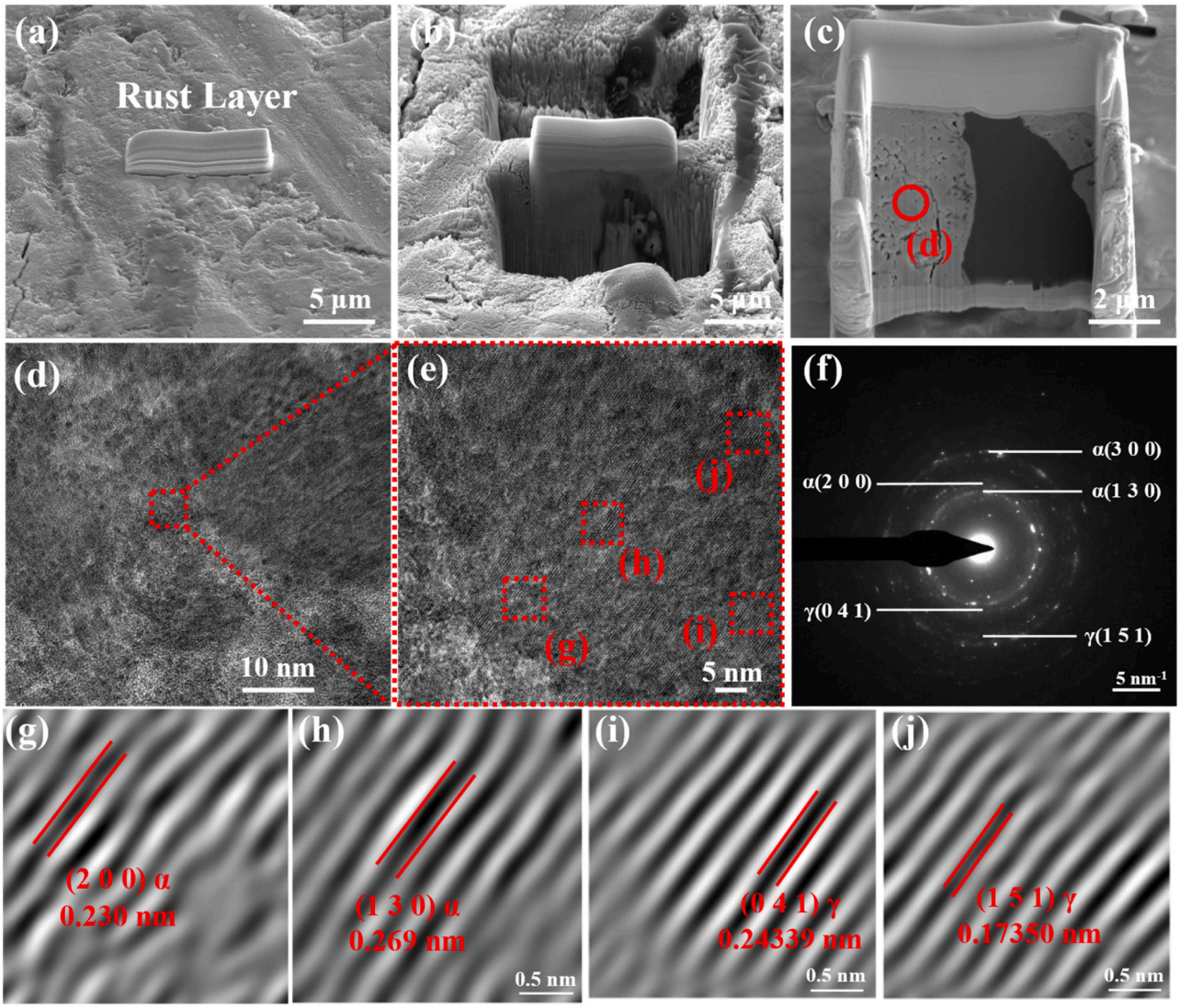

Fig. 11. (a) Selected rust layer location on the blank sample; (b-c) 3D morphology of the rust layer on the blank sample; (d-e) TEM images of the red-marked region in (c); (f) SAED pattern corresponding to (e); (g–j) Fourier transform (FFT) pattern maps of the selected regions in (e).

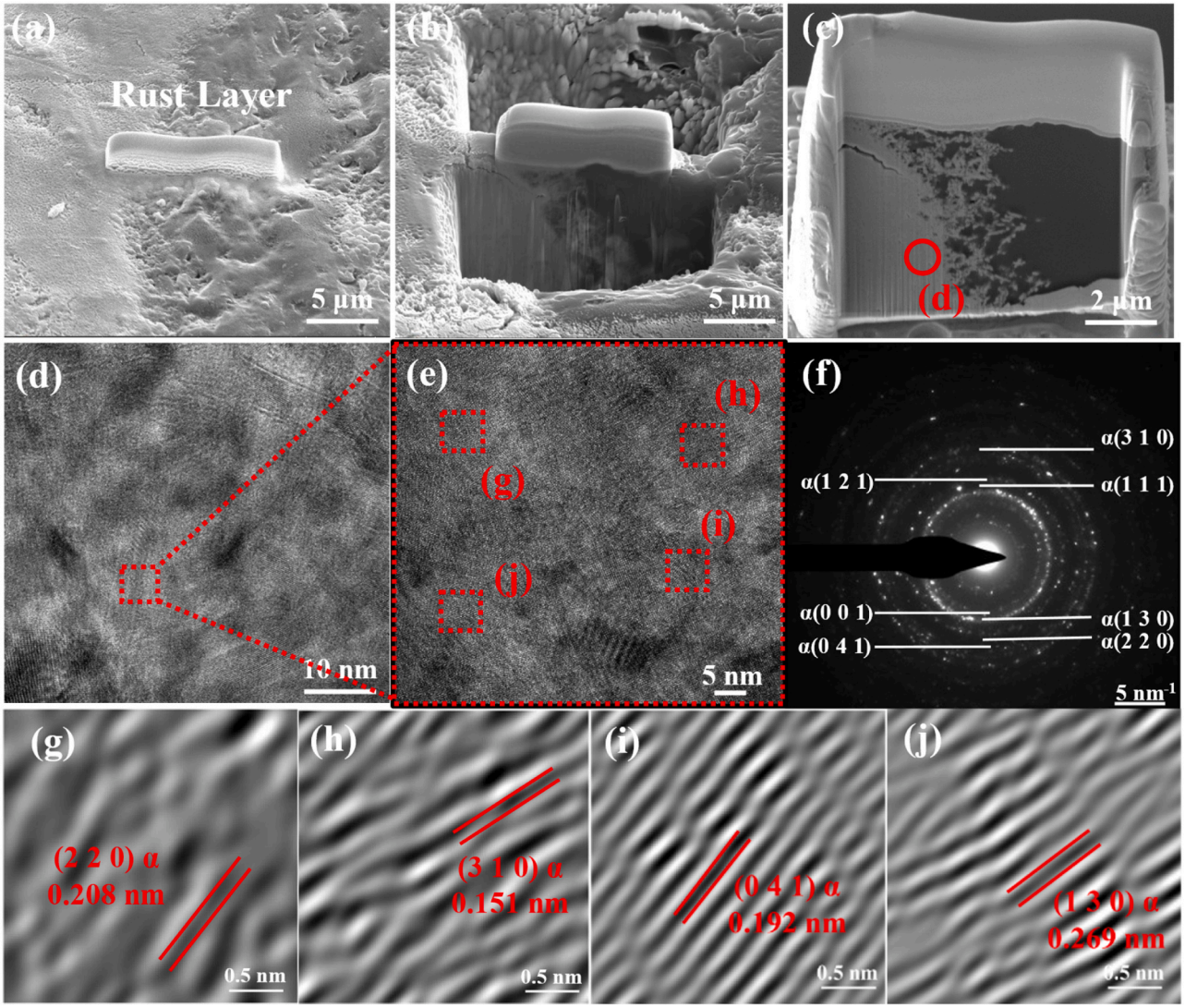

Fig. 12. (a) Selected rust layer location on the pre-treated sample; (b-c) 3D morphology of the rust layer on the blank sample; (d-e) TEM images of the red-marked region in (c); (f) SAED pattern corresponding to (e); (g–j) Fourier transform (FFT) pattern maps of the selected regions in (e).

the penetration of corrosive media [58,60]. This observation, combined with the relatively uniform grain arrangement shown in the bright-field TEM images, suggests that the rust layer in the pre-treated sample favors the improved corrosion resistance.

3.7. Mechanism of rust layer formation treat by STA on WS

Under natural conditions, WS undergoes an electrochemical corrosion process: Fe dissolves at the anode to yield Fe^{2+}, while dissolved oxygen is reduced at the cathode. The Fe^{2+} produced then hydrates to form FeO and $Fe(OH)_2$. With the progress of corrosion, the iron ions undergo further oxidation to generate corrosion products such as γ-FeOOH, α-FeOOH, Fe_2O_3, and Fe_3O_4 [48,61,62]. Without surface treatment, the naturally formed rust layer on WS consists mainly of γ-FeOOH and α-FeOOH, with the α-FeOOH present in only small amounts, which leads to accelerated corrosion of WS during outdoor exposure. For the surface treatment of WS, the use of STA is one of the key measures. It can effectively accelerate the formation of rust layer, increase its stability, and enhance the overall corrosion resistance of the steel. $CuSO_4$, $MgSO_4$, Na_2HPO_4, and TA can improve the stability and protection performance of WS rust layer through the enhancement mechanism. Specifically, $CuSO_4$ induces a displacement reaction that deposits metallic Cu within the rust layer, creating numerous weak cathodes to refine rust layer grains, and promoting the formation of stable α-FeOOH phase [14,63]. The SO_4^{2-} ions from $MgSO_4$ and $CuSO_4$ accelerate early dissolution of the steel substrate, facilitating initial γ-FeOOH formation and expediting rust layer development [14]. Na_2HPO_4 can react with Fe^{2+} to form a dense iron-phosphate protective film, suppressing unstable rust phases while improving the adhesion and compactness of the rust layer [13,17]. TA with polyphenolic structure can chelate Fe^{3+} ions to generate stable complexes, markedly enhancing the uniformity and density of the rust layer [18]. When these four STA components are used in combination, their individual advantages are cumulatively enhanced, resulting in a more stable and compact rust layer, thereby significantly enhancing the corrosion resistance of WS under complex corrosive environments.

4. Conclusion

In this study, we developed an integrated method that combines high-throughput experimentation, interpretable ML, and Bayesian optimization to design and optimize rust layer STA for WS. This approach notably reduced experimental demands, efficiently identifying the optimal STA formulation from over 2825761 possibilities with just 79 experiments:

1) ML modeling using the AdaBoost algorithm achieved high prediction accuracy, with an R^2 value of 0.93 on the test set after iterative enhancements, ensuring robust and reliable prediction of $|Z|_{0.01\ Hz}$.
2) Interpretability analysis provided critical insights, highlighting significant contributions from SO_4^{2-} and Cu^{2+} ions, identifying their optimal concentration ranges as 0.4–0.6 g/L and 0.2–0.5 g/L respectively, thus guiding precise component optimization.
3) Bayesian optimization leveraged these insights to pinpoint the optimal STA formulation:0.70 g/L $CuSO_4$, 0.20 g/L $MgSO_4$, 0.60 g/L Na_2HPO_4, and 0.20 g/L tannic acid, which yielded a maximum experimental impedance of 35.8 kΩ·cm², surpassing the initial results by 47.0 %.
4) Experimental validation demonstrated the optimized formulation's superiority. Analyses revealed that after pretreatment, the rust layer exhibited reduced defects, diminished chloride penetration, increased Cu enrichment, and a higher proportion of stable α-FeOOH phase, thereby enhancing the overall corrosion resistance.

CRediT authorship contribution statement

Xin Guo: Writing – review & editing, Conceptualization. **Zongbao Li:** Data curation, Conceptualization. **Lingwei Ma:** Writing – review & editing, Supervision, Resources, Project administration. **Yiran Li:** Writing – original draft, Visualization, Methodology. **Dawei Zhang:** Supervision, Resources, Conceptualization. **Arjan Mol:** Supervision, Methodology. **Jinke Wang:** Investigation, Formal analysis. **Jingzhi Yang:** Investigation, Data curation.

Declaration of Competing Interest

The authors declare that they have no known competing financial interests or personal relationships that could have appeared to influence the work reported in this paper.

Acknowledgements

This work is financially supported by the National Natural Science Foundation of China (No. 52522102, 52371049), the Beijing Nova Program (No. 20250484763), the Open Research Foundation of Southwest Technology and Engineering Research Institute (grant number HDHDW59CZ), and the computing work is supported by the Open Source Supercomputing Center of S-A-I.

Appendix A. Supporting information

Supplementary data associated with this article can be found in the online version at doi:10.1016/j.corsci.2025.113494.

Data availability

Data will be made available on request.

References

[1] M. Morcillo, I. Díaz, B. Chico, H. Cano, D. de la Fuente, Weathering steels: from empirical development to scientific design. A review, Corros. Sci. 83 (2014) 6–31, https://doi.org/10.1016/j.corsci.2014.03.006.
[2] X. Cheng, Z. Jin, M. Liu, X. Li, Optimizing the nickel content in weathering steels to enhance their corrosion resistance in acidic atmospheres, Corros. Sci. 115 (2017) 135–142, https://doi.org/10.1016/j.corsci.2016.11.016.
[3] M. Morcillo, B. Chico, I. Díaz, H. Cano, D. de la Fuente, Atmospheric corrosion data of weathering steels. A review, Corros. Sci. 77 (2013) 6–24, https://doi.org/10.1016/j.corsci.2013.08.021.
[4] B. Shi, L. Qin, D. Xu, X. Cheng, C. Liu, G. Yang, F. Xu, X. Li, Exploring corrosion protection evolution of rust layer on high-Cr-content weathering bridge steel in simulated tropical marine atmosphere, Int. J. Miner. Metall. Mater. (2024), https://doi.org/10.1007/s12613-024-3069-3.
[5] X.Q. Cheng, Y.W. Tian, X.G. Li, C. Zhou, Corrosion behavior of nickel-containing weathering steel in simulated marine atmospheric environment, (n.d.). https://doi.org/10.1002/maco.201307447.
[6] W. Wu, Z. Dai, Z. Liu, C. Liu, X. Li, Synergy of Cu and Sb to enhance the resistance of 3%Ni weathering steel to marine atmospheric corrosion, Corros. Sci. 183 (2021) 109353, https://doi.org/10.1016/j.corsci.2021.109353.
[7] M. Sun, C. Du, Z. Liu, C. Liu, X. Li, Y. Wu, Fundamental understanding on the effect of Cr on corrosion resistance of weathering steel in simulated tropical marine atmosphere, Corros. Sci. 186 (2021) 109427, https://doi.org/10.1016/j.corsci.2021.109427.
[8] Q. Hu, S. Yang, X. Zhang, G. Da, W. Zhang, Accelerating stabilization of weathering steel through rust modification pre-corrosion treatment, Heliyon 10 (2024), https://doi.org/10.1016/j.heliyon.2023.e23842.
[9] J. Gao, W. Xu, B. Zhang, C. Li, G. Li, B. Hou, Protective mechanism and stabilization treatment technology of rust layer on weathering steel in atmospheric environments, J. Eng. Sci. 47 (2025) 1032–1046, https://doi.org/10.13374/j.issn2095-9389.2024.07.12.001.
[10] G. Zhou, T. Guo, X. Yi, X. Nan, W. Wu, Y. Hu, Effect of semi-permeable film stabilisation treatment on dry and wet cyclic corrosion behaviour of Q420qENH weathering steel plates and welded joints in deicing salt media, Surf. Coat. Technol. 485 (2024) 130925, https://doi.org/10.1016/j.surfcoat.2024.130925.
[11] Q. Yu, B. Li, F. Wang, J. Tai, P. Liu, The role of stabilization technology on the enhancement of corrosion resistance and corrosion mechanism for weathering steel, Mater. Today Commun. 40 (2024) 109694, https://doi.org/10.1016/j.mtcomm.2024.109694.
[12] D.C. Cook, The corrosion of high performance steel in adverse environments, AIP Conf. Proc. 765 (2005) 63–72, https://doi.org/10.1063/1.1923636.
[13] S. Ma, L. Sun, H. Sun, H. Sun, J. Jiang, Y. Yin, S. Qu, Z. Liu, S. Xu, Stabilization technology and corrosion mechanism of rust layer on Q370 weathering steel surface, J. Iron. Steel Res. Int. 29 (2022) 1694–1709, https://doi.org/10.1007/s42243-022-00819-y.
[14] M. Fan, K. Zhao, J. Ke, J. Yang, X. Liu, D. Luo, C. Fan, X. Xiong, Q. Chen, F. Li, W. Zhang, E. Ghali, H. Guo, Effect of sulfate-based stabilizers on the rust layer formation and corrosion resistance of Q420qNH weathering steel, Mater. Corros. n/a (n.d.). https://doi.org/10.1002/maco.202414640.
[15] H. Cano, D. Neff, M. Morcillo, P. Dillmann, I. Diaz, D. de la Fuente, Characterization of corrosion products formed on Ni 2.4wt%–Cu 0.5wt%–Cr 0.5wt % weathering steel exposed in marine atmospheres, Corros. Sci. 87 (2014) 438–451, https://doi.org/10.1016/j.corsci.2014.07.011.
[16] I. Díaz, H. Cano, P. Lopesino, D. de la Fuente, B. Chico, J.A. Jiménez, S.F. Medina, M. Morcillo, Five-year atmospheric corrosion of Cu, Cr and Ni weathering steels in a wide range of environments, Corros. Sci. 141 (2018) 146–157, https://doi.org/10.1016/j.corsci.2018.06.039.
[17] L. Hao, S. Zhang, J. Dong, W. Ke, Atmospheric corrosion resistance of MnCuP weathering steel in simulated environments, Corros. Sci. 53 (2011) 4187–4192, https://doi.org/10.1016/j.corsci.2011.08.028.
[18] B. Qian, B. Hou, M. Zheng, The inhibition effect of tannic acid on mild steel corrosion in seawater wet/dry cyclic conditions, Corros. Sci. 72 (2013) 1–9, https://doi.org/10.1016/j.corsci.2013.01.040.
[19] C. Ren, L. Ma, X. Luo, C. Dong, T. Gui, B. Wang, X. Li, D. Zhang, High-throughput assessment of corrosion inhibitor mixtures on carbon steel via droplet microarray, Corros. Sci. 213 (2023) 110967, https://doi.org/10.1016/j.corsci.2023.110967.
[20] X. Guo, X. Ding, Y. Wang, J. Wang, W. Tan, Y. Li, Z. Chen, Z. Li, W. Chen, L. Ma, D. Zhang, High-throughput screening of green amino acid and surfactant mixtures with high corrosion inhibition efficiency: experimental and modelling perspectives, Corros. Sci. 240 (2024) 112460, https://doi.org/10.1016/j.corsci.2024.112460.
[21] Z. Li, L. Ma, C. Ren, J. Wang, R. Tian, Z. Chen, W. Chen, X. Li, D. Zhang, Accelerated rust stabilization for weathering steels via a high-throughput approach, Corros. Sci. 244 (2025) 112645, https://doi.org/10.1016/j.corsci.2024.112645.
[22] J. Recatala-Gomez, A. Suwardi, I. Nandhakumar, A. Abutaha, K. Hippalgaonkar, Toward accelerated thermoelectric materials and process discovery, ACS Appl. Energy Mater. 3 (2020) 2240–2257, https://doi.org/10.1021/acsaem.9b02222.
[23] K. Kaufmann, K.S. Vecchio, Searching for high entropy alloys: a machine learning approach, Acta Mater. 198 (2020) 178–222, https://doi.org/10.1016/j.actamat.2020.07.065.
[24] F. Ren, L. Ward, T. Williams, K.J. Laws, C. Wolverton, J. Hattrick-Simpers, A. Mehta, Accelerated discovery of metallic glasses through iteration of machine learning and high-throughput experiments, Sci. Adv. (2018), https://doi.org/10.1126/sciadv.aaq1566.
[25] C. Ren, L. Ma, D. Zhang, X. Li, A. Mol, High-throughput experimental techniques for corrosion research: a review, Mater. Genome Eng. Adv. 1 (2023) e20, https://doi.org/10.1002/mgea.20.
[26] H. Meng, J. Huang, T. Zhao, X. Zhang, Y. Tong, J. Qu, W. Li, L. Jiang, F. Meng, S. Chen, High-throughput assessment of Nb, Co, Ti, and Al effects on microstructure and mechanical properties in wrought nickel-based superalloys, Mater. Genome Eng. Adv. n/a (n.d.) e70002. https://doi.org/10.1002/mgea.70002.
[27] S. Zhao, J. Li, W. Liao, R. Yuan, Machine learning-guided plasticity model in refractory high-entropy alloys, Mater. Genome Eng. Adv. 3 (2025) e70022, https://doi.org/10.1002/mgea.70022.
[28] Y. Shi, Y. Zhang, J. Wen, Z. Cui, J. Chen, X. Huang, C. Wen, B. Sa, Z. Sun, Interpretable machine learning for stability and electronic structure prediction of janus III–VI van der waals heterostructures, Mater. Genome Eng. Adv. 2 (2024) e76, https://doi.org/10.1002/mgea.76.
[29] J. Yang, Y. Ran, S. Liu, C. Ren, Y. Lou, P. Ju, G. Li, X. Li, D. Zhang, Synergistic D-amino acids based antimicrobial cocktails formulated via high-throughput

screening and machine learning, Adv. Sci. 11 (2024) 2307173, https://doi.org/10.1002/advs.202307173.
[30] B. Shi, X. Guo, L. Wang, W. Huang, H. Luo, L. Qin, G. Yang, X. Cheng, X. Li, Multi-objective optimization of corrosion resistance, strength, ductility properties of weathering steel utilizing interpretable attention-based deep learning model, Npj Mater. Degrad. 9 (2025) 103, https://doi.org/10.1038/s41529-025-00654-y.
[31] J. Noh, H.A. Doan, H. Job, L.A. Robertson, L. Zhang, R.S. Assary, K. Mueller, V. Murugesan, Y. Liang, An integrated high-throughput robotic platform and active learning approach for accelerated discovery of optimal electrolyte formulations, Nat. Commun. 15 (2024) 2757, https://doi.org/10.1038/s41467-024-47070-5.
[32] M. Suvarna, T. Zou, S.H. Chong, Y. Ge, A.J. Martín, J. Pérez-Ramírez, Active learning streamlines development of high performance catalysts for higher alcohol synthesis, Nat. Commun. 15 (2024) 5844, https://doi.org/10.1038/s41467-024-50215-1.
[33] G. Tom, S.P. Schmid, S.G. Baird, Y. Cao, K. Darvish, H. Hao, S. Lo, S. Pablo-García, E.M. Rajaonson, M. Skreta, N. Yoshikawa, S. Corapi, G.D. Akkoc, F. Strieth-Kalthoff, M. Seifrid, A. Aspuru-Guzik, Self-driving laboratories for chemistry and materials science, Chem. Rev. 124 (2024) 9633–9732, https://doi.org/10.1021/acs.chemrev.4c00055.
[34] Q.L. Thu, G. Bonnet, C. Compere, H.L. Trong, S. Touzain, Modified wire beam electrode: a useful tool to evaluate compatibility between organic coatings and cathodic protection, Prog. Org. Coat. 52 (2005) 118–125, https://doi.org/10.1016/j.porgcoat.2004.10.002.
[35] G. Cai, S. Xiao, C. Deng, D. Jiang, X. Zhang, Z. Dong, CeO2 grafted carbon nanotube via polydopamine wrapping to enhance corrosion barrier of polyurethane coating, Corros. Sci. 178 (2021) 109014, https://doi.org/10.1016/j.corsci.2020.109014.
[36] Y. Wu, Y. Ke, Z. Chen, S. Liang, H. Zhao, H. Hong, Application of alternating decision tree with AdaBoost and bagging ensembles for landslide susceptibility mapping, Catena 187 (2020) 104396, https://doi.org/10.1016/j.catena.2019.104396.
[37] A. Natekin, A. Knoll, Gradient boosting machines, a tutorial, Front. Neurorob. 7 (2013), https://doi.org/10.3389/fnbot.2013.00021.
[38] L. Breiman, Random forests, Mach. Learn 45 (2001) 5–32, https://doi.org/10.1023/A:1010933404324.
[39] T. Chen, C. Guestrin, XGBoost: a scalable tree boosting system. Proceedings of the 22nd ACM SIGKDD International Conference on Knowledge Discovery and Data Mining, Association for Computing Machinery, New York, NY, USA, 2016, pp. 785–794, https://doi.org/10.1145/2939672.2939785.
[40] Y. Zhi, Z. Jin, L. Lu, T. Yang, D. Zhou, Z. Pei, D. Wu, D. Fu, D. Zhang, X. Li, Improving atmospheric corrosion prediction through key environmental factor identification by random forest-based model, Corros. Sci. 178 (2021), https://doi.org/10.1016/j.corsci.2020.109084.
[41] B. Wang, Y. Mu, F. Shen, R. Zhu, Y. Li, C. Liu, X. Cheng, D. Zhang, X. Li, Identification of corrosion factors in blast furnace gas pipe network with corrosion big data online monitoring technology, Corros. Sci. 230 (2024) 111906, https://doi.org/10.1016/j.corsci.2024.111906.
[42] D. Xue, P.V. Balachandran, J. Hogden, J. Theiler, D. Xue, T. Lookman, Accelerated search for materials with targeted properties by adaptive design, Nat. Commun. 7 (2016) 11241, https://doi.org/10.1038/ncomms11241.
[43] P. Liu, H. Huang, C. Wen, T. Lookman, Y. Su, The γ/γ′ microstructure in CoNiAlCr-based superalloys using triple-objective optimization, Npj Comput. Mater. 9 (2023), https://doi.org/10.1038/s41524-023-01090-9.
[44] J. Ma, B. Cao, S. Dong, Y. Tian, M. Wang, J. Xiong, S. Sun, MLMD: a programming-free AI platform to predict and design materials, Npj Comput. Mater. 10 (2024) 1–12, https://doi.org/10.1038/s41524-024-01243-4.
[45] W. Wu, X. Cheng, J. Zhao, X. Li, Benefit of the corrosion product film formed on a new weathering steel containing 3% nickel under marine atmosphere in Maldives, Corros. Sci. 165 (2020) 108416, https://doi.org/10.1016/j.corsci.2019.108416.
[46] X. Guo, L. Ma, Z. Fu, J. Wang, Z. Li, B. Shi, Y. Li, G. Yang, L. Lu, D. Zhang, Molecular understanding of the effects of electrode potential and electric double layer on the adsorption process of two azole-based corrosion inhibitors, Corros. Sci. 253 (2025) 112991, https://doi.org/10.1016/j.corsci.2025.112991.
[47] X. Guo, X. Zhang, L. Ma, Y. Li, J. Le, Z. Fu, L. Lu, D. Zhang, Understanding the adsorption of imidazole corrosion inhibitor at the copper/water interface by ab initio molecular dynamics, Corros. Sci. 236 (2024) 112237, https://doi.org/10.1016/j.corsci.2024.112237.
[48] W. Wu, Z. Zeng, X. Cheng, X. Li, B. Liu, Atmospheric corrosion behavior and mechanism of a Ni-advanced weathering steel in simulated tropical marine environment, J. Mater. Eng. Perform. 26 (2017) 6075–6086, https://doi.org/10.1007/s11665-017-3043-6.
[49] T. Zhang, W. Liu, Z. Yin, B. Dong, Y. Zhao, Y. Fan, J. Wu, Z. Zhang, X. Li, Effects of the addition of Cu and Ni on the corrosion behavior of weathering steels in corrosive industrial environments, J. Mater. Eng. Perform. 29 (2020) 2531–2541, https://doi.org/10.1007/s11665-020-04738-5.
[50] M. Ates, K. Yilmaz, A. Shahryari, S. Omanovic, A.S. Sarac, A study of the electrochemical behavior of poly [N-vinyl carbazole] formed on carbon-fiber microelectrodes and its response to dopamine, IEEE Sens. J. 8 (2008) 1628–1639, https://doi.org/10.1109/JSEN.2008.929069.
[51] Y. Ma, Y. Li, F. Wang, Corrosion of low carbon steel in atmospheric environments of different chloride content, Corros. Sci. 51 (2009) 997–1006, https://doi.org/10.1016/j.corsci.2009.02.009.
[52] A. Carnot, I. Frateur, S. Zanna, B. Tribollet, I. Dubois-Brugger, P. Marcus, Corrosion mechanisms of steel concrete moulds in contact with a demoulding agent studied by EIS and XPS, Corros. Sci. 45 (2003) 2513–2524, https://doi.org/10.1016/S0010-938X(03)00076-3.
[53] T. Zhang, W. Liu, L. Chen, B. Dong, W. Yang, Y. Fan, Y. Zhao, On how the corrosion behavior and the functions of Cu, Ni and Mo of the weathering steel in environments with different NaCl concentrations, Corros. Sci. 192 (2021) 109851, https://doi.org/10.1016/j.corsci.2021.109851.
[54] J. Alcántara, B. Chico, J. Simancas, I. Díaz, D. De La Fuente, M. Morcillo, An attempt to classify the morphologies presented by different rust phases formed during the exposure of carbon steel to marine atmospheres, Mater. Charact. 118 (2016) 65–78, https://doi.org/10.1016/j.matchar.2016.04.027.
[55] Y. Yang, T. Lin, G. Wang, Y. Wang, M. Shao, F. Meng, F. Wang, Corrosion behaviors of weathering steels in the actual marine atmospheric zone and immersion zone, Metals 14 (2024) 903, https://doi.org/10.3390/met14080903.
[56] Y. Wang, J. Li, Q. Wang, T. Wang, Some new discoveries on the structure of the rust layer of weathering steel in a simulated industrial atmosphere by STEM-EDS and HRTEM, Corros. Sci. 183 (2021) 109322, https://doi.org/10.1016/j.corsci.2021.109322.
[57] Y. Wang, J. Li, L. Zhang, L. Zhang, Q. Wang, T. Wang, Structure of the rust layer of weathering steel in a high chloride environment: a detailed characterization via HRTEM, STEM-EDS, and FIB-SEM, Corros. Sci. 177 (2020) 108997, https://doi.org/10.1016/j.corsci.2020.108997.
[58] L. Qin, B. Shi, F. Xu, X. Cheng, C. Liu, D. Xu, X. Li, Effect of Sn on the rust layer structure of new high-Cr-content steels in a high chloride ion concentration environment, Mater. Charact. 224 (2025) 114981, https://doi.org/10.1016/j.matchar.2025.114981.
[59] B. Shi, L. Sun, L. Wang, Z. He, X. Guo, H. Luo, X. Cheng, N. Jia, X. Li, Simultaneously enhancing the mechanical properties and corrosion resistance of FeMnCoCr high-entropy alloy via N-doping, J. Mater. Sci. Technol. (2025), https://doi.org/10.1016/j.jmst.2025.06.052.
[60] L. Sun, Z. He, N. Jia, Y. Guo, S. Jiang, Y. Yang, Y. Liu, X. Guan, Y. Shen, H.-L. Yan, P.K. Liaw, Local chemical order enables an ultrastrong and ductile high-entropy alloy in a cryogenic environment, Sci. Adv. 10 (2024) eadq6398, https://doi.org/10.1126/sciadv.adq6398.
[61] Y. Sun, W. Liu, Z. Sun, H. Li, B. Zhang, W. Yang, L. Chen, B. Dong, T. Zhang, Optimizing microstructure for enhanced atmospheric corrosion resistance of a novel Ni–Mo weathering steel: a field exposure study in Thailand's tropical marine environment, Vacuum 221 (2024) 112876, https://doi.org/10.1016/j.vacuum.2023.112876.
[62] Y. Sun, W. Liu, B. Dong, T. Zhang, L. Chen, W. Yang, H. Li, B. Zhang, J. Xie, J. Cui, Designing weathering steel with optimized Mo/Ni ratios for better corrosion resistance in simulated tropical marine atmosphere, Met. Mater. Int. 30 (2024) 909–927, https://doi.org/10.1007/s12540-023-01547-y.
[63] K.-T. Kim, H. Tsuchiya, K. Hanaki, M. Yamashita, S. Fujimoto, Effect of cations on protective properties of rust layer formed on carbon steel during wet/dry cyclic corrosion, Mater. Trans. 61 (2020) 506–514, https://doi.org/10.2320/matertrans.MT-M2019270.